Dual-Comb Mid-Infrared Spectromicroscopy with Photothermal Fluorescence Detection

Short Title: Dual-Comb IR Photothermal Fluorescence Microscopy

Gwendylan A. Turner,[1] Daniel I. Herman,[2] Aleksandr Razumtcev,[1] Markus Mangold,[2] Minghe Li,[1] Ziyi Cao,[1] Jiayue Rong,[1] Charles A. Bouman,[3] Gregery Buzzard[4], Garth J. Simpson[1*]

[1]Department of Chemistry, Purdue University, West Lafayette IN 47907

[2]IRsweep AG, Stäfa, Switzerland 8712

[3]Department of Electrical and Computer Engineering, Purdue University, West Lafayette IN 47907

[4]Department of Mathematics, Purdue University, West Lafayette IN 47907

gsimpson@purdue.edu

Abstract: An approach is described for spectrally parallel hyperspectral mid-infrared imaging with spatial resolution dictated by fluorescence imaging. Quantum cascade laser (QCL)-based dual-comb mid-infrared spectroscopy enables acquisition of infrared spectra at high speed (<1 millisecond) through generation of optical beat patterns and radio-frequency detection. The high-speed nature of the spectral acquisition is shown to support spectral mapping in microscopy measurements. Direct detection of the transmitted infrared beam yields high signal-to-noise spectral information, but the long infrared wavelength imposes low diffraction-limited spatial resolution. Use of fluorescence detected photothermal infrared (F-PTIR) imaging provides high spatial resolution tied directly to the integrated IR absorption. Computational imaging using a multi-agent consensus equilibrium (MACE) approach combines the high spatial resolution of F-PTIR and the high spectral information of dual-comb infrared transmission in a single optimized equilibrium hyperspectral data cube.

Teaser: Instrumentation and computational methods push both temporal and spatial limits of infrared spectromicroscopy.

Introduction

Infrared spectroscopy is one of the most powerful analytical tools for chemical fingerprinting and materials characterization. Recent advancements in dual-comb instrumentation have expanded the application-space of IR spectroscopy by circumventing traditional limits on speed, sensitivity, and spatial resolution for imaging spectrometers. The working principle of dual-comb mid-infrared (DC-IR) utilizes a pair of broad-band infrared frequency combs with close, but nonidentical, comb repetition frequencies. Heterodyne detection and Fourier transformation of the dual-comb time-domain beat patterns (interferograms) allow recovery of infrared absorption spectra with microsecond time resolution. Difference frequency generation (DFG) in a nonlinear medium is widely used for the generation of individual infrared combs. However, the introduction and commercial availability of high-power mid-IR quantum cascade lasers (QCLs) (*1*) have aided successful generation of QCL-based optical frequency combs (*2*), and these advancements have resulted in the recent development of QCL-based dual comb spectrometers exhibiting sub-wavenumber fidelity(*3*) For both sources, the DC-IR technique enables parallel detection across all IR wavelengths, suppressing 1/f noise from slow drift and removing Poynting vector walk associated with frequency swept QCL sources. The fast acquisition rate of DC-IR spectrometers has enabled the time-resolved study of protein dynamics (*4*), the fast monitoring of biochemical processes (*5*), and the study of molecular adsorption/desorption (*6*). Additionally, several modalities of DC spectroscopy have been implemented, with research groups demonstrating DC spectroscopy via photoacoustic (*7, 8*) and photothermal (*9*) detection.

The high temporal resolution of DC-IR spectroscopy raises supports the possibility of fast, chemically specific, mid-IR spectroscopic imaging. While imaging has been explored through proof-of concept using DFG-based DC-IR (*10, 11*), QCL-based DC-IR imaging has not been demonstrated in the

literature to date. Rapid advances in QCL sources have substantially improved the accessibility of QCL comb technology and its integration into dual comb systems, with access to broader spectral ranges than those easily achievable with (DFG)-based DC-IR (*12*). These advances in fast, broadband, and accessible sources have set the stage for expansion of DC-IR for the characterization of heterogeneous, complex systems in chemistry and biology. However, the relatively low spatial resolution inherent in infrared transmission/reflection imaging remains a limiting barrier in practical applications. In biological applications, the diffraction-limited spatial resolution in the mid-infrared is on the same order as the size of a single cell, preventing meaningful access to sub-cellular structural features critical to understanding biological processes.

Addressing the diffraction-limited resolution limit in far-field infrared chemical imaging remains an open challenge. A number of promising strategies based on computational imaging methods were attempted previously. Assuming the point-spread function of the imaging system is known, deconvolution methods, such as Fourier self-deconvolution and total variation, can be employed to increase the spatial resolution of IR imaging systems (*13–15*). However, implementation of classical deconvolution methods remains limited in accuracy due to experimental realities such as scattering, glare, and blur, particularly in imaging within the turbid or spatially structured samples that are routinely characterized in microscopy measurements. (*16*) Once lost, computational recovery of high frequency content in the presence of measurement noise is generally an ill-posed operation requiring an exceptionally high signal to noise ratio. Hence, a union between innovative approaches in instrumentation hardware design and purely computational strategies is needed to further push the boundaries of sub-diffraction hyperspectral imaging in the mid-IR range.

One of the promising recent efforts in addressing the existing limitations of infrared imaging is optical photothermal infrared (O-PTIR) microscopy that uses an additional tightly focused visible laser beam to probe local temperature variations in the sample associated with infrared absorption. One of the most recent O-PTIR modalities, fluorescence-detected photothermal mid-infrared (F-PTIR) microscopy leverages the thermal sensitivity of the fluorescence quantum yield and was independently demonstrated in 2021 by Li *et al.* (*17*) and by Zhang *et al.* (*18*) This new modality provides simpler PSFs and ~100-fold signal-to-noise improvement as compared to previously established detection scheme based on refractive index modulation (*19–24*). Following initial establishment, researchers have demonstrated further improvements and broad application ranges of F-PTIR microscopy including label-free imaging based on intrinsic UV autofluorescence emission of small molecules and protein crystals (*25*), fast 3D volumetric imaging (*26*), and discrimination between crystal polymorph forms using QCL spectral masking (*27*). Due to its high sensitivity and improved selectivity enabled by fluorescence labeling, F-PTIR is particularly promising as a potential modality for integration with dual-comb infrared sources. It should be noted that the change in fluorescence intensity in F-PTIR is driven by the IR absorption in the matrix surrounding the fluorophore at length scales on the order of hundreds of nanometers, differing it from several recent studies that demonstrated fluorescence-detected vibrational spectroscopy of single fluorescent molecules based on nonlinear double resonance excitation schemes, including fluorescence-encoded IR (*28*), and Raman (*29*) spectroscopies, as well as BonFIRE imaging (*30*).

In this work, we not only demonstrate QCL-based DC-IR imaging in the mid-IR range, but we also achieve hyperspectral high-resolution mid-IR microscopy through the integration of DC-IR dual comb source with a custom FPTIR microscope. DC-IR was used for fast sample-scanning hyperspectral imaging with high spectral but low spatial resolution, while complementary photothermal microscopy provided high spatial resolution but spectrally broadband absorption maps. A multi-agent consensus equilibrium (MACE) algorithm for computational imaging was adapted for hyperspectral image reconstruction and used to merge the two imaging modalities (*31–33*). The equilibrium output of MACE balanced the cost functions inherent within each of the two imaging methods (DC-IR and F-PTIR) to create a hyperspectral image cube with both high spatial and spectral resolution. The present proof-of-concept demonstration of DC-IR imaging opens new prospects for the development of fast hyperspectral imaging in the fingerprint region with high spatial, spectral, and temporal resolution.

Materials and Methods

DC-FPTIR Microscope

The dual comb F-PTIR microscope consisted of a commercially available QCL dual-comb spectroscopy (DCS) system (IRis-core, IRsweep, Switzerland) co-propagated with a 532 nm diode laser (LOCLasers -GL532) for fluorescence excitation. The IR and probe beams were combined using a germanium window (Thorlabs WG91050-G) and focused onto the sample plane with a ZnSe aspherical lens (Edmund Optics, 39-469).

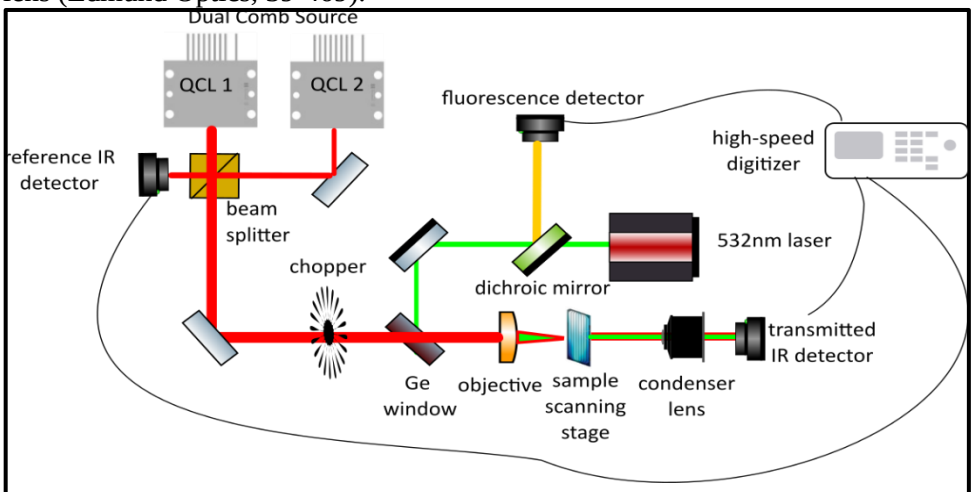

Figure 1: Instrument schematic for DC-F-PTIR and IR transmission measurements. A Dual-Comb QCL Source is combined with a 532 nm laser via a germanium window and focused with a zinc selenide refractive objective, with fluorescence measured in the back-propagating (epi) direction.

As illustrated in **Figure 1,** IR transmission measurements of the DCS through the sample were accomplished with a pair of fast mid-infrared detectors (Vigo), with one serving as a reference detector located prior to the IR-visible beam combination and the other as a transmitted IR detector after the sample. Dual comb spectra composed of 200 spectral elements between 1035 cm^{-1} and 1085 cm^{-1} and were taken with a single pixel acquisition time of 260 microseconds. For hyperspectral imaging, a piezoelectric scanning stage (MadCityLabs NanoBio 300) provided positional sample scanning across a 125 µm by 250 µm field of view (8100 pixels). Hyperspectral data were acquired through pixel-by-pixel high-speed digitization. It is worth noting that the speed of hyperspectral image acquisition was limited not by infrared spectral scanning, but by digitization speed, delivering a total time of 40 seconds per image for all IR transmission images presented herein. A line-by-line digitization scheme presented in the supplementary information was found to reduce total acquisition time to a stage-limited acquisition time of 10 seconds. Images obtained with this digitization method are presented in the supplementary information.

Fluorescence signal was acquired with a photomultiplier tube (PMT) assembly in epi-detection (Hamamatsu H10721-210) where fluorescence is reflected to via a 550 nm short-pass dichroic mirror (Thorlabs) and subsequently filtered using a 532 nm notch (Thorlabs), and a 550 nm (Thorlabs) long-pass filters. For F-PTIR imaging, a chopper at a modulation frequency of 200 Hz was introduced in the IR beam path, and fluorescence was detected using the aforementioned PMT detector. The sample was scanned through the same field of view with a total acquisition time of 150 seconds per image, and the reference of the chopper was collected to transduce the modulated fluorescence image. Thus, the collected F-PTIR image represents the integrated photothermal modulation across the entire infrared range.

Sample preparation and characterization

Hydrated Rhodamine-6G (R6G) – associated silica gel samples were prepared through manual mortar-and-pestle grinding of silica gel and subsequent dissolution of silica gel and rhodamine 6-G in deionized water . The water evaporated over 24 hours, and the remaining particles were placed onto a calcium fluoride (CaF_2) slide for imaging. Polydextran samples were prepared by dissolving rhodamine B-

labeled polydextran (10,000 M.W., ThermoFischer Scientific) in deionized water, which was deposited onto a calcium fluoride slide and left to dry for 24 hours.

To evaluate acquired DCS spectra, attenuated total reflectance (ATR) spectra of the pure sample components were taken with a Thermo Nicolet 6700 FT-IR spectrometer for reference.

Hyperspectral Data Fusion

Merging of the hyperspectral DC-IR image cube with fluorescence and F-PTIR measurements was performed using a custom multi-agent consensus equilibrium (MACE) approach, written in-house in Matlab. In brief, MACE operates to identify a single hyperspectral image cube striking an optimal balance between the constraints imposed by the DC-IR (high spectral and low spatial resolution) and F-PTIR (low spectral and high spatial resolution) measurements. MACE for computational image reconstruction (*31–35*) serves as a foundation for the work presented herein, the detailed underpinnings of which are presented in the Supplementary Information, with a graphical illustration depicted in **Figure S1**.

Results

DC-IR Transmission Hyperspectral Imaging

Dual comb infrared transmission measurements are shown in **Figure 2** for a sample consisting of silica gel-particles infused with Rhodamine-6G fluorescent dye. The signal to noise ratio (SNR) within one pixel was noteworthy, with detectable changes of a few parts per 1000 in %T. This SNR was achieved with a single pixel integration time of 260 μs for the DC-IR measurements and is consistent with prior reports for DC-IR (*12*). The transmitted IR from a representative single pixel contains sharp features with a periodicity of ~5 cm^{-1}, which are attributed to etalon interference effects from the co-parallel planar surfaces of the CaF_2 substrate. Transmittance spectra were obtained following normalization by a featureless region within the

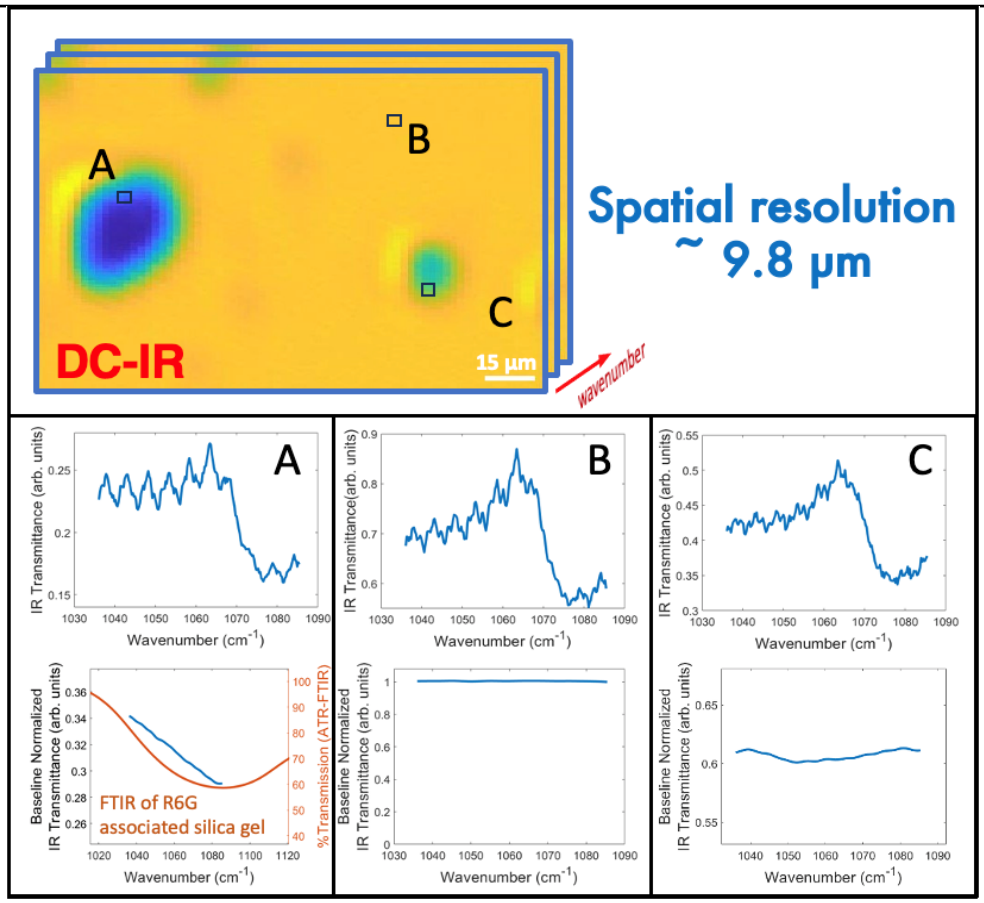

Figure 2: Raw DC-IR hyperspectral image stack of R6G-associated silica gel particles. A representative image is shown for a single infrared wavelength (1070 cm^{-1}), and resolution is estimated through the derivative of a line scan across the edge of the leftmost particle. Both unnormalized (top) and normalized (bottom) spectra of indicated locations are provided for single pixels in the corresponding panels (A-C). The unnormalized spectra are dominated by etalon effects originating from the parallel planar surfaces of the calcium fluoride substrate, as evidenced by qualitatively similar patterns emerging indiscriminately across the field of view. Normalization to a featureless region in the field of view results in a phase shift of the etalon in featured regions A and C. For comparison to an ATR FT-IR spectrum, the spectra presented in the bottom of each panel were Gaussian smoothed by 6.5cm^{-1} (2σ).

field of view, and though the normalization successfully eliminated the etalon within the featureless regions, it did not successfully account for the phase shift in the short-range etalon effect introduced by the change in surface and path length across featured regions.

While the DC-IR measurements yield exquisite sensitivity in the spectral domain, the long wavelength inherent in IR spectroscopy results in relatively low spatial resolution. Cross-sectional analysis of the particles shown in **Figure 2** enables estimation of the spatial resolution. Treating the particles as comprising sharp knife-edges, the resolution can be estimated directly from the derivative of a line-scan across the particle edge. This approach provides a lower bound on the spatial resolution, yielding the correct spatial resolution only for particles exhibiting sharp edges with "flat-top" intensity profiles. Based on this analysis, the minimum resolvable distance of the DC-IR image of silica gel was found to be 9.8µm. This value is less resolved than the diffraction-limited value of 5.7 µm, given by the numerical aperture (NA) of the aspherical lens (1.00) and the IR wavelength (1070cm^{-1}); however, this value is well aligned with performances previously reported in DFG-based DC-IR microscopy(*10, 11*), and the spatial resolution may suffer depending on the degree of spatial overlap of the two combs at the sample plane. Additionally, the resolution reported below is prone to underestimate the resolution due to departures from flat-top profiles in infrared absorption. In either case, it is far below the spatial resolution routinely achieved in optical microscopy using visible light.

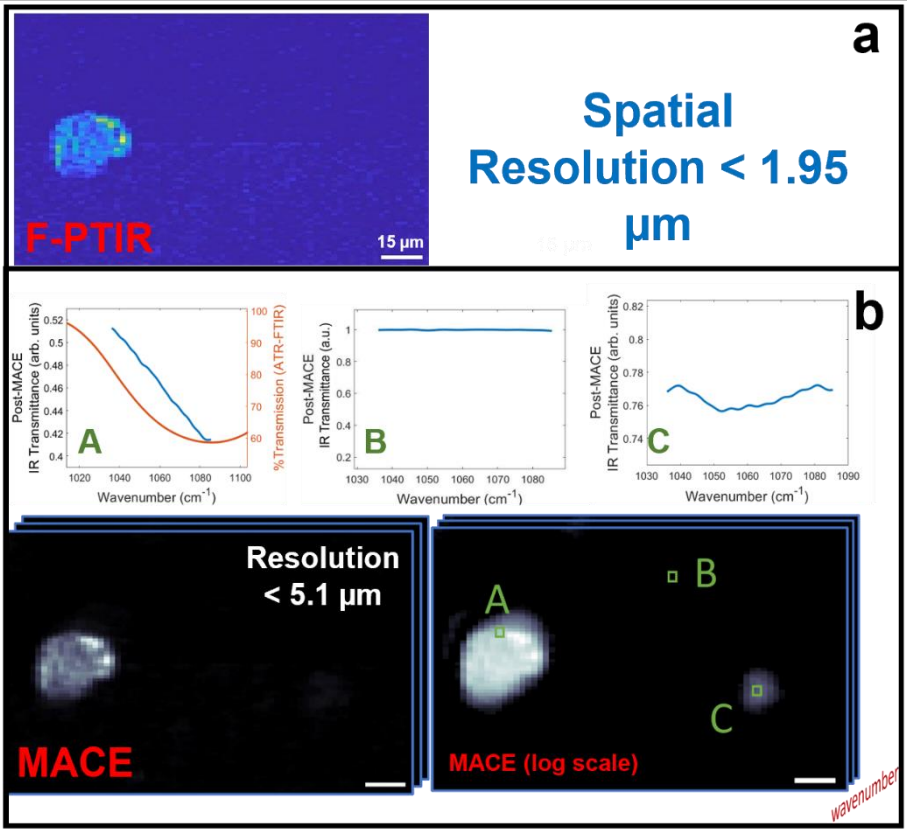

Figure 3: (a) – An F-PTIR image of the fluorescent silica gel sample collected by demodulating the fluorescence at the frequency corresponding to the chopping of the entire DC-IR QCL beam. (b) – Results of MACE fusion of the high-resolution F-PTIR image with low resolution hyperspectral DC-IR cube. Both a linear (left) and logarithmic scaling images are shown to highlight the unchanged resolution quality of the non-fluorescent particle on the bottom right. Spectral results for representative locations are shown in corresponding panels.

F-PTIR and Fluorescence Imaging

Fluorescence-detected photothermal infrared (F-PTIR) microscopy was performed to improve on the spatial resolution in infrared absorption microspectroscopy relative to direct IR transmission detection, the result of which is shown in **Figure 3a**. In F-PTIR, the IR absorption is transduced through a corresponding thermal modulation in the fluorescence intensity. This approach leverages a high intrinsic sensitivity of the fluorescence quantum efficiency with temperature, with many common fluorescent dyes yielding emission intensity reductions of 1-2 %/^{o}C. Relative to direct detection of the transmitted IR, F-PTIR has the potential to yield substantial improvements in spatial resolution. Consistent with this expectation, spatial resolution in the F-PTIR image was limited by pixelation effects to <2 µm rather than from the optical point spread function.

Modulation of the dual-comb source using an optical chopper provided high modulation depths for F-PTIR detection, with all IR wavelengths within the emission bandwidth of the QCL pair contributing to

the measured modulation in fluorescence. However, much of the detailed spectral information within the IR beam was lost in this manner, as the F-PTIR in this configuration integrated over the absorption measured simultaneously at all wavelengths within the QCL bandwidth. As such F-PTIR yielded excellent spatial resolution but limited spectral information, in direct contrast to DC-IR measurements.

Computational Merging with Multi-Agent Consensus Equilibrium (MACE)

The highly complementary information content from DC-IR and F-PTIR are well-suited for computational imaging methods for data fusion, the results of which are shown in **Figure 3b** evaluated using MACE. In MACE, a balance is struck between the inherent cost structure within each agent, producing a net equilibrium output that, under favorable conditions, retains the features from which deviation is most costly. Both DC-IR and F-PTIR were cast as agents designed to output hyperspectral data cubes in a commonly shared hyperspectral "MACE-space".

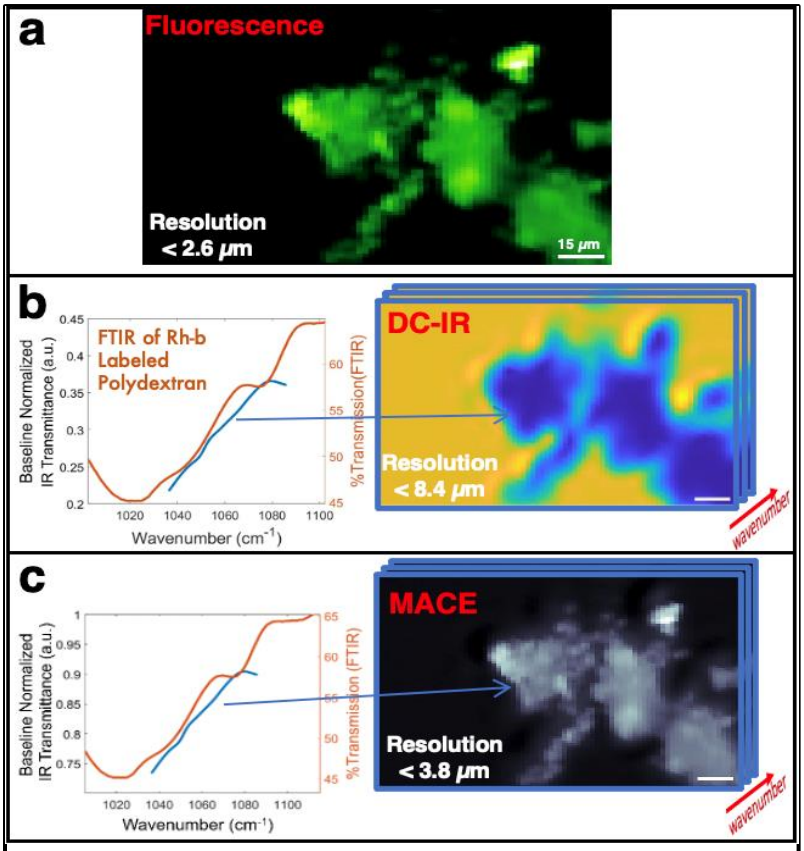

Figure 4. (a) – High-resolution fluorescence image of a FoV containing RhB-labeled polydextran particles. (b) – Transmission DC-IR image and representative normalized DCIR spectrum at the indicated location overlayed with ATR-FTIR spectrum (orange). (c) - Post-MACE computationally merged image and representative post-MACE spectrum of normalized, gaussian smoothed spectra 6cm^{-1} (2σ) overlayed with ATR-FTIR spectrum.

Consistent with expectations for MACE, the equilibrium DC-F-PTIR hypercube retains both the high spatial resolution of F-PTIR and the high spectral resolution of DC-IR. Using the same knife-edge method described previously, the DC-F-PTIR hypercube exhibited a spatial resolution of 5.12 μm (compared to ~10 μm for DC-IR). Furthermore, the fluorescent domains yielded negligible differences between the per-pixel DC-IR spectra and the MACE spectra at those same locations.

Upon rescaling the brightness axis of the combined DC-F-PTIR map, low-amplitude features appear at locations with detectable attenuation of the IR in DC-IR from serendipitous particles that did not exhibit detectable fluorescence but produced IR absorption. Those regions are indicated in **Figure 3b** and exhibit distinct differences in their IR spectra. It is worth highlighting that the MACE algorithm used to merge the DC-IR and F-PTIR results retains these features despite their absence in the F-PTIR image.

While the F-PTIR measurements provide a rigorous bridge between connecting the infrared absorption with high-resolution fluorescence microscopy, in principle any high-resolution image contrast mechanism could potentially aid in resolution improvement by MACE. To test this conjecture, additional MACE calculations were performed to computationally merge high-resolution fluorescence micrographs with low spatial resolution, high spectral resolution DC-IR images, the results of which are shown in **Figure 4** for rhodamine-labeled polydextran conglomerate particles. Despite the absence of a clear dependence of the fluorescence image on IR absorption, the high-resolution fluorescence micrograph nevertheless serves

as an effective guide-star in the IR spatial deconvolution operation within the MACE algorithm. After MACE, the minimum resolvable distance was improved from 8.4 μm for DC-IR to 3.8 μm calculated using the same knife-edge approach detailed above. These results suggest analogous potential benefits from integration of other high-resolution measurements, including bright-field images. These trends are in good qualitative agreement with prior hyperspectral IR imaging studies by Phal *et al*. (*36*). In that work, computational reconstruction of infrared transmission hyperspectral images resulted in resolution at long infrared wavelengths effectively set by the contrast from the shortest wavelength windows in the hyperspectral image cube. However, the visible probe beam used in F-PTIR and fluorescence microscopy is an order of magnitude shorter in wavelength than the blue edge of the infrared spectral window used in the previous hyperspectral IR imaging work, corresponding to substantial improvements in spatial resolution.

Discussion

Instrumentation and computational methods are described to enable DC-IR hyperspectral imaging with spatial resolution below the infrared diffraction limit. These initial proof-of-concept results set the stage for a broad suite of applications in biology and materials analysis of heterogeneous assemblies, leveraging the high speed and spectral sensitivity of DC-IR with spatially resolved analysis in optical microscopy. To our knowledge, these results represent the first demonstration of DC-IR imaging in the vibrational "fingerprint" spectral range between ~500 cm^{-1} to ~1500cm^{-1}. MACE was realized as a tool for computational merging of hyperspectral infrared image cubes with either photothermal or fluorescence images. Both MACE outputs yielded spatial resolutions higher than the calculated diffraction limits for the mid-infrared wavelengths utilized here. Computational integration of DC-IR hyperspectral imaging with F-PTIR allowed localization of the IR absorption with sub-diffraction limited spatial resolution and negligible loss in spectral accuracy. These collective results demonstrate a pathway to enable QCL-based DC-IR microscopy with high spatial resolution and rich hyperspectral information in the fingerprint IR spectral range. This realization of high spatial and spectral mid-infrared DC-IR imaging sets the stage for future studies of the local chemical environment around site-specific fluorescent labels in biologically important samples.

In principle, photothermal fluorescence detection at radio frequencies characteristic of the QCL dual-comb system could chemically inform on the local environment immediately adjacent to the fluorescence reporter, enabling co-localization analysis over distances shorter even than the visible diffraction limit. Frequencies in the megahertz regime would correspond to colocalization distances on the order of nanometers, which represents a future opportunity for photothermal fluorescence spectroscopy.

Acknowledgements

The authors gratefully acknowledge funding for the present work from the National Science Foundation (CHE-2004046, CHE-2305178, CHE-2320751, CIF-1763896). DIH and MM acknowledge financial support from IRsweep AG to support these collaborative studies. This work was also supported in part by the Research Instrumentation Center in the Department of Chemistry at Purdue University.

References

1. J. Faist, F. Capasso, D. L. Sivco, C. Sirtori, A. L. Hutchinson, A. Y. Cho, Quantum Cascade Laser. *Science (1979)* **264**, 553–556 (1994).
2. A. Hugi, G. Villares, S. Blaser, H. C. Liu, J. Faist, Mid-infrared frequency comb based on a quantum cascade laser. *Nature 2012 492:7428* **492**, 229–233 (2012).

3. M. Lepère, O. Browet, J. Clément, B. Vispoel, P. Allmendinger, J. Hayden, F. Eigenmann, A. Hugi, M. Mangold, A mid-infrared dual-comb spectrometer in step-sweep mode for high-resolution molecular spectroscopy. *J Quant Spectrosc Radiat Transf* **287**, 108239 (2022).
4. L. Schubert, P. Langner, D. Ehrenberg, V. A. Lorenz-Fonfria, J. Heberle, Protein conformational changes and protonation dynamics probed by a single shot using quantum-cascade-laser-based IR spectroscopy. *Journal of Chemical Physics* **156**, 204201 (2022).
5. M. J. Norahan, R. Horvath, N. Woitzik, P. Jouy, F. Eigenmann, K. Gerwert, C. Kötting, Microsecond-Resolved Infrared Spectroscopy on Nonrepetitive Protein Reactions by Applying Caged Compounds and Quantum Cascade Laser Frequency Combs. *Anal Chem* **93**, 6779–6783 (2021).
6. E. Lins, S. Read, B. Unni, S. M. Rosendahl, I. J. Burgess, Microsecond Resolved Infrared Spectroelectrochemistry Using Dual Frequency Comb IR Lasers. *Anal Chem* **92**, 6241–6244 (2020).
7. J. T. Friedlein, E. Baumann, K. A. Briggman, G. M. Colacion, F. R. Giorgetta, A. M. Goldfain, D. I. Herman, E. V. Hoenig, J. Hwang, N. R. Newbury, E. F. Perez, C. S. Yung, I. Coddington, K. C. Cossel, Dual-comb photoacoustic spectroscopy. *Nature Communications 2020 11:1* **11**, 1–10 (2020).
8. T. Wildi, T. Voumard, V. Brasch, G. Yilmaz, T. Herr, Photo-acoustic dual-frequency comb spectroscopy. *Nature Communications 2020 11:1* **11**, 1–6 (2020).
9. Q. Wang, Z. Wang, H. Zhang, S. Jiang, Y. Wang, W. Jin, W. Ren, Dual-comb photothermal spectroscopy. *Nature Communications 2022 13:1* **13**, 1–7 (2022).
10. P. Chang, N. Hoghooghi, S. Swartz, D. Lesko, R. Ishrak, S. Egbert, J. Biegert, R. Reddy, G. Rieker, S. Diddams, Mid-Infrared Hyperspectral Microscopy with Broadband 1-GHz Dual-Comb Spectroscopy. *CLEO 2023 (2023), paper SM3O.2*, SM3O.2 (2023).
11. H. Timmers, A. Kowligy, A. J. Lind, N. Nader, J. Shaw, D. Zalvidea, J. Biegert, S. A. Diddams, Hyperspectral Microscopy with Broadband Infrared Frequency Combs. *Conference on Lasers and Electro-Optics (2019), paper SF1E.4* (2019).
12. G. Ycas, F. R. Giorgetta, E. Baumann, I. Coddington, D. Herman, S. A. Diddams, N. R. Newbury, High-coherence mid-infrared dual-comb spectroscopy spanning 2.6 to 5.2 µm. *Nature Photonics 2018 12:4* **12**, 202–208 (2018).
13. P. Lasch, D. Naumann, Spatial resolution in infrared microspectroscopic imaging of tissues. *Biocimica et Biophysica Acta (BBA) Biomembranes* **1758** (2006).
14. T. P. Wrobel, R. Bhargava, Infrared Spectroscopic Imaging Advances as an Analytical Technology for Biomedical Sciences HHS Public Access. *Anal Chem* **90**, 1444–1463 (2018).
15. F. Lai, J. Kandukuri, B. Yuan, Z. Zhang, M. Jin, Thermal Image Enhancement through the Deconvolution Methods for Low-Cost Infrared Cameras. doi: 10.1080/17686733.2018.1441956.
16. M. Makarkin, D. Bratashov, State-of-the-Art Approaches for Image Deconvolution Problems, including Modern Deep Learning Architectures. *Micromachines 2021, Vol. 12, Page 1558* **12**, 1558 (2021).
17. M. Li, A. Razumtcev, R. Yang, Y. Liu, J. Rong, A. C. Geiger, R. Blanchard, C. Pfluegl, L. S. Taylor, G. J. Simpson, Fluorescence-Detected Mid-Infrared Photothermal Microscopy. *J Am Chem Soc* **143**, 10809–10815 (2021).
18. Y. Zhang, H. Zong, C. Zong, Y. Tan, M. Zhang, Y. Zhan, J. X. Cheng, Fluorescence-Detected Mid-Infrared Photothermal Microscopy. *J Am Chem Soc* **143**, 11490–11499 (2021).
19. I. M. Pavlovetc, E. A. Podshivaylov, R. Chatterjee, G. V. Hartland, P. A. Frantsuzov, M. Kuno, Infrared photothermal heterodyne imaging: Contrast mechanism and detection limits. *J Appl Phys* **127**, 165101 (2020).
20. J. Yin, M. Zhang, Y. Tan, Z. Guo, H. He, L. Lan, J. X. Cheng, Video-rate mid-infrared photothermal imaging by single-pulse photothermal detection per pixel. *Sci Adv* **9**, eadg8814 (2023).

21. M. S. Ünlü, J. X. Cheng, J. H. Connor, Y. Zhang, C. Yurdakul, A. J. Devaux, L. Wang, X. G. Xu, Vibrational spectroscopic detection of a single virus by mid-infrared photothermal microscopy. *Anal Chem* **93**, 4100–4107 (2021).
22. V. Beltran, A. Marchetti, G. Nuyts, M. Leeuwestein, C. Sandt, F. Borondics, K. De Wael, Nanoscale Analysis of Historical Paintings by Means of O-PTIR Spectroscopy: The Identification of the Organic Particles in L'Arlésienne (Portrait of Madame Ginoux) by Van Gogh. *Angewandte Chemie International Edition* **60**, 22753–22760 (2021).
23. J. Yin, L. Lan, Y. Zhang, H. Ni, Y. Tan, M. Zhang, Y. Bai, J. X. Cheng, Nanosecond-resolution photothermal dynamic imaging via MHZ digitization and match filtering. *Nature Communications 2021 12:1* **12**, 1–11 (2021).
24. Y. Su, X. Hu, H. Tang, K. Lu, H. Li, S. Liu, B. Xing, R. Ji, Steam disinfection releases micro(nano)plastics from silicone-rubber baby teats as examined by optical photothermal infrared microspectroscopy. *Nature Nanotechnology 2021 17:1* **17**, 76–85 (2021).
25. A. Razumtcev, M. Li, J. Rong, C. C. Teng, C. Pfluegl, L. S. Taylor, G. J. Simpson, Label-Free Autofluorescence-Detected Mid-Infrared Photothermal Microscopy of Pharmaceutical Materials. *Anal Chem* **94**, 6512–6520 (2022).
26. D. Jia, Y. Zhang, Q. Yang, Y. Xue, Y. Tan, Z. Guo, M. Zhang, L. Tian, J.-X. Cheng, 3D Chemical Imaging by Fluorescence-detected Mid-Infrared Photothermal Fourier Light Field Microscopy. doi: 10.1021/cbmi.3c00022.
27. A. Razumtcev, M. Li, G. J. Simpson, Parts-per-Million Detection of Trace Crystal Forms Using AF-PTIR Microscopy. *Anal Chem* **94**, 13100–13107 (2022).
28. L. Whaley-Mayda, A. Guha, S. B. Penwell, A. Tokmakoff, Fluorescence-Encoded Infrared Vibrational Spectroscopy with Single-Molecule Sensitivity. *J Am Chem Soc* **143**, 3060–3064 (2021).
29. H. Xiong, L. Shi, L. Wei, Y. Shen, R. Long, Z. Zhao, W. Min, Stimulated Raman excited fluorescence spectroscopy and imaging. *Nat Photonics* **13**, 412–417 (2019).
30. H. Wang, D. Lee, Y. Cao, X. Bi, J. Du, K. Miao, L. Wei, Bond-selective fluorescence imaging with single-molecule sensitivity. *Nat Photonics* **17**, 846–855 (2023).
31. G. T. Buzzard, S. H. Chan, S. Sreehari, C. A. Bouman, Plug-and-Play Unplugged: Optimization-Free Reconstruction Using Consensus Equilibrium. *https://doi.org/10.1137/17M1122451* **11**, 2001–2020 (2018).
32. E. J. Reid, L. F. Drummy, C. A. Bouman, G. T. Buzzard, Multi-Resolution Data Fusion for Super Resolution Imaging. *IEEE Trans Comput Imaging* **8**, 81–95 (2022).
33. S. Majee, T. Balke, C. Kemp, G. Buzzard, C. Bouman, Multi-Slice Fusion for Sparse-View and Limited-Angle 4D CT Reconstruction. *IEEE Trans Comput Imaging* **7**, 448–461 (2021).
34. V. Sridhar, X. Wang, G. T. Buzzard, C. A. Bouman, Distributed Iterative CT Reconstruction Using Multi-Agent Consensus Equilibrium. *IEEE Trans Comput Imaging* **6**, 1153–1166 (2020).
35. X. Wang, V. Sridhar, Z. Ronaghi, R. Thomas, J. Deslippe, D. Parkinson, G. T. Buzzard, S. P. Midkiff, C. A. Bouman, S. K. Warfield, Consensus equilibrium framework for super-resolution and extreme-scale CT reconstruction. *International Conference for High Performance Computing, Networking, Storage and Analysis, SC*, doi: 10.1145/3295500.3356142 (2019).
36. Y. Phal, L. Pfister, P. S. Carney, R. Bhargava, Resolution Limit in Infrared Chemical Imaging. *J. Phys. Chem. C* **2022**, 9777–9783 (2022).
37. J. R. W. Ulcickas, Z. Cao, J. Rong, C. A. Bouman, L. v. Slipchenko, G. T. Buzzard, G. J. Simpson, Multiagent Consensus Equilibrium in Molecular Structure Determination. *J Phys Chem A* **124**, 9105–9112 (2020).
38. W. R. Mann, Mean value methods in iteration. *Proceedings of the American Mathematical Society* **4**, 506–510 (1953).